Received 29 October 2021; revised 10 December 2021; accepted 19 December 2021. Date of publication 28 December 2021; date of current version 12 January 2022. The review of this article was arranged by Associate Editor Xin (GAE) Zhang.

Digital Object Identifier 10.1109/OJPEL.2021.3138509

Stability Assessment of A Radial Grid With Power Converters

XINGQI LIU [1] (Student Member, IEEE), ZHIXIANG ZOU [1] (Senior Member, IEEE), JIAJUN YANG [2] (Student Member, IEEE), JIAN TANG[1], ZHIREN LIU[3], GIAMPAOLO BUTICCHI [2] (Senior Member, IEEE), ZHENG WANG[1] (Senior Member, IEEE), AND MING CHENG [1] (Fellow, IEEE)

[1]Southeast University, Nanjing 210096, China
[2]University of Nottingham Ningbo China, Ningbo 315100, China
[3]State Grid Wuxi Power Supply Company, Wuxi 214062, China

CORRESPONDING AUTHOR: ZHIXIANG ZOU (e-mail: zzou@seu.edu.cn)

This work was supported in part by the National Natural Science Foundation of China under Grant 52007033, and in part by the State Grid Jiangsu Electric Power Co., Ltd., under Grant J2021210.

ABSTRACT The increase proportion of power converters causes stability problems in the radial grid. To address these issues, this paper firstly proposes a unified modeling procedure and applies it to two types of converters. Secondly, the impedance models are used to analyze the stability of a radial grid with converters under four cases. The influence of the short circuit ratio (SCR) and line impedance on system stability are investigated. Then, a comprehensive sensitivity analysis is performed in order to investigate the effects of parameters variations on the closed-loop poles of the system under different conditions. Finally, the accuracy of the model and theoretical analysis are verified by simulations and Hardware-in-the-Loop (HiL) tests.

INDEX TERMS Radial grid, grid-following converter, grid-forming converter, impedance model, complex frequency domain, stability, sensitivity analysis.

I. INTRODUCTION

With the development of renewable energy generation system, the penetration of power converters in a radial grid increases significantly, which causes modeling and stability issues [1]. The existing research mainly uses small signal modeling method to model converters. This method can be divided into two categories: time domain modeling method based on the state space model and frequency domain modeling method based on the impedance model [2]. The establishment of the state space model requires the detailed structure and parameters of converters. At present, some manufacturers keep the internal structure and parameters of the converter confidentially, it is difficult to obtain the complete state space model of converters. Compared to the state space model, the impedance model is a more direct and easier method which can be obtained either from the detailed parameters or the measured terminal characteristics. Thus, the impedance model has drawn extensive attention. In [4]–[7], the impedance model of grid-following converter was proposed on considering the influence of phase-locked loop (PLL). In [8], the simplified impedance model of grid-following converters was studied which simplifies the modeling procedure. In [9], the unified modeling method of grid-following converter under three-phase balance and three-phase unbalance condition was studied. In [10], the impedance model of grid-forming converter adopting droop control strategy was analyzed and impedance measurement was used to verify its correctness. In [11], [12], for grid-forming converter adopting droop control strategy, phase angle was seen as an input and the transfer function among voltage, current and phase angle was analyzed. However, in the existing literature, each model is valid for the specific type of converters with specific control strategy. The general modeling model methodology is still missing.

Based on the impedance model of converters, many researchers study the stability of the distribution grid with converters. In [13], the stability indices and margins of two grid-following converters with different parameters, particularly with different PLL bandwidths and power injections were studied and it provided a general design guideline of PLL bandwidths of two converters. In [14], the stability on different types of converters respectively connected to the PLL-based converter was studied and μ-analysis was firstly proposed to assess system robust stability. In [15], the interactions mechanism between two PLL-synchronization converters operating in parallel was studied. In [16], the eigenvalue analysis and component connection method (CCM) were used to analysis parallel system contains the PLL-based converter and the synchronverter. In [17], the system contained three parallel grid-following converters system under different operating conditions was studied. At present, most of researches focus on the influence of identical type of converters on the stability of grids, while the system stability containing different kinds of converters has been seldom investigated. Moreover, the sensitivity analysis of impedance of power converters in a radial grid is still missing.

In this respect, this paper aims to study the stability of a radial grid on considering the influence of different types of converters and line impedance. The contributions of this paper include:

1) Unified modeling procedure is proposed and applied to two types of converters;
2) Stability issues for a radial grid with different types of converters under different cases are investigated;
3) Parameter sensitivity analysis for a two-bus radial grid with different types of converters is performed.

The paper structure is organized as follows. The classification of power converter is introduced in Section II. The unified modeling procedure is proposed and is applied to the two types of converters in Section III. The influence of line parameters on system stability under four cases and parameter sensitivity are studied in Section IV. The developed model and theoretical analysis are verified by simulations and Hardware-in-the-Loop (HiL) tests in Section V. Conclusions are drawn in Section VI.

II. CLASSIFICATION OF POWER CONVERTER

According to control strategies, power converters are classified into two categories: grid-following converter and grid-forming converter [21], [22].

A. GRID-FOLLOWING CONVERTER

Grid-following converter typically uses PLL and current loop to achieve rapid control of the converters' output current. Due to its output characteristic, the grid-following converter is equivalent to an ideal AC current source in parallel with an admittance connecting to the grid. The simplified equivalent model is shown in Fig. 1(a).

B. GRID-FORMING CONVERTER

Grid-forming converter adjusts output active and reactive power by controlling voltage magnitude and frequency. It is equivalent to an ideal AC voltage source in series with an impedance, and its simplified equivalent model is shown in Fig. 1(b). Typical power control strategies of grid-forming converters include: droop control, VSG, and synchronous power controller (SPC) [23].

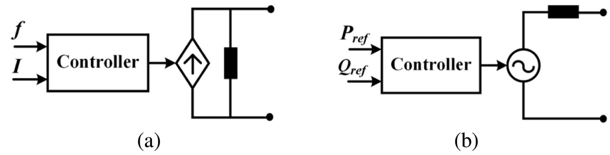

FIGURE 1. **Simplified equivalent models of power converters: (a) grid-following converter, (b) grid-forming converter.**

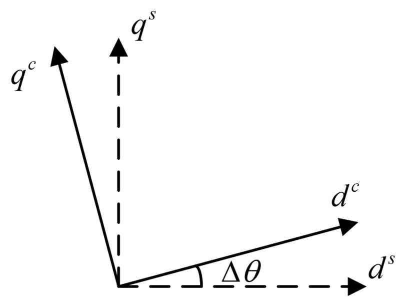

FIGURE 2. **Relationship between system d-q axis and controller d-q axis.**

III. UNIFIED MODELING PROCEDURE OF POWER CONVERTERS

For grid-following converters, PLL provides phase angle. For grid-forming converters, power loop (or power-based synchronization) provides phase angle. Phase angle will affect the Park transform and its inverse. Thus, the system has two d-q reference frames. One is grid side d-q frame, which is synchronized with the grid voltage, and the other is synchronized with the phase angle provided by PLL or power loop. When a small-signal perturbation is added to PCC voltage, the two d-q frames no longer overlap, which results in an angle difference $\Delta\theta$ as shown in Fig. 2. Voltage and current in two frames satisfy the following relationship [4]:

$$\begin{bmatrix} x_d^c \\ x_q^c \end{bmatrix} = \begin{bmatrix} \cos(\Delta\theta) & \sin(\Delta\theta) \\ -\sin(\Delta\theta) & \cos(\Delta\theta) \end{bmatrix} \begin{bmatrix} x_d^s \\ x_q^s \end{bmatrix} \tag{1}$$

The superscript c represents the vector under the d-q frame on the controller side, and the superscript s represents vector under the d-q frame on the grid side. x represents v, i, v_c, v_r, $i_L$which are shown in Figs. 3 and 5.

According to (1), the relationship between the components on both sides is shown in (2).

$$\begin{aligned} \begin{bmatrix} X_d^c + \Delta x_d^c \\ X_q^c + \Delta x_q^c \end{bmatrix} &= \begin{bmatrix} \cos(\Delta\theta) & \sin(\Delta\theta) \\ -\sin(\Delta\theta) & \cos(\Delta\theta) \end{bmatrix} \begin{bmatrix} X_d^s + \Delta x_d^s \\ X_q^s + \Delta x_q^s \end{bmatrix} \\ &\approx \begin{bmatrix} 1 & \Delta\theta \\ -\Delta\theta & 1 \end{bmatrix} \begin{bmatrix} X_d^s + \Delta x_d^s \\ X_q^s + \Delta x_q^s \end{bmatrix} \end{aligned} \tag{2}$$

where X_d and X_q represent steady-state quantities. Δx_d and Δx_q represent small-signal disturbances.

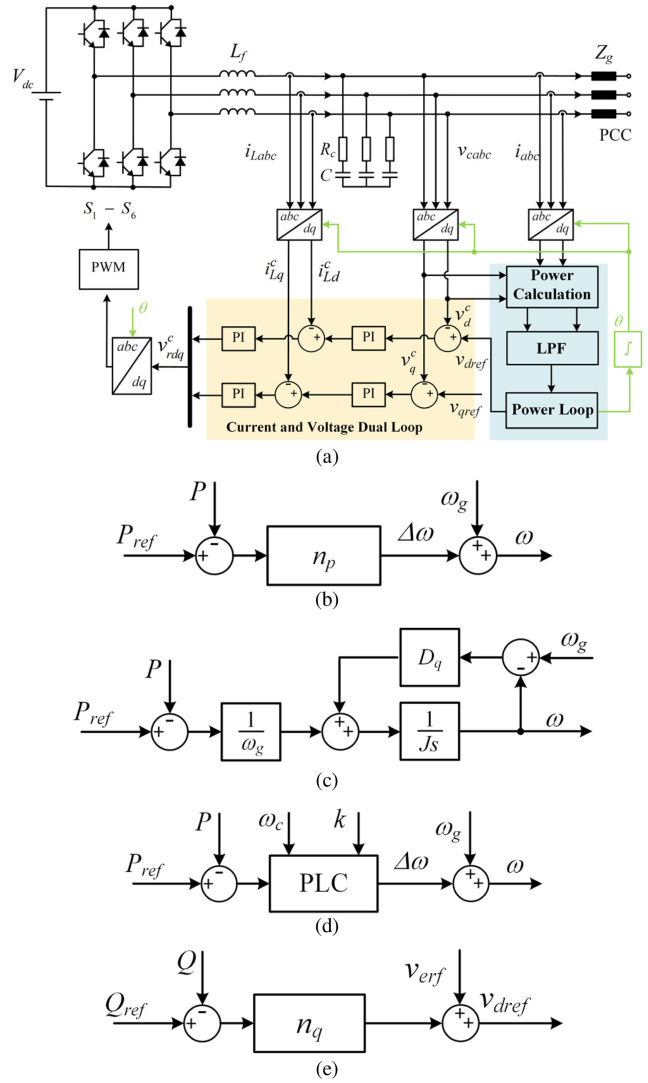

FIGURE 3. Configuration of the grid-forming converter: (a) Typical system configuration [11], (b) Droop control active power loop [11], (c) VSG active power loop [24], (d) SPC active power loop [25], (e) reactive power loop [11].

Simplifying (2), one can get

$$\begin{bmatrix} \Delta x_d^c \\ \Delta x_q^c \end{bmatrix} = \begin{bmatrix} \Delta x_d^s + \Delta\theta X_q^s \\ \Delta x_q^s - \Delta\theta X_d^s \end{bmatrix} \tag{3}$$

$\Delta\theta$ has a functional relationship with its input vector. For grid-following converter, it has relationship with Δv_q^c. For grid-forming converter, it has relationship with converter's output voltage and current. Thus the functional relationship between $\Delta\theta$ and its input can be established as shown below.

$$\Delta\theta = \begin{bmatrix} G_{1d} & G_{1q} \end{bmatrix} \begin{bmatrix} \Delta Y_{1d} \\ \Delta Y_{1q} \end{bmatrix} + \begin{bmatrix} G_{2d} & G_{2q} \end{bmatrix} \begin{bmatrix} \Delta Y_{2d} \\ \Delta Y_{2q} \end{bmatrix} \tag{4}$$

where Y_1 and Y_2 are input of $\Delta\theta$.

Substitute (4) into (3)

$$\begin{bmatrix} \Delta x_d^c \\ \Delta x_q^c \end{bmatrix} = \begin{bmatrix} \Delta x_d^s \\ \Delta x_q^s \end{bmatrix} + \begin{bmatrix} G_{1d} X_q^s & G_{1q} X_q^s \\ -G_{1d} X_d^s & -G_{1q} X_d^s \end{bmatrix} \begin{bmatrix} \Delta Y_{1d} \\ \Delta Y_{1q} \end{bmatrix} + \begin{bmatrix} G_{2d} X_q^s & G_{2q} X_q^s \\ -G_{2d} X_d^s & -G_{2q} X_d^s \end{bmatrix} \begin{bmatrix} \Delta Y_{2d} \\ \Delta Y_{2q} \end{bmatrix} \tag{5}$$

Based on (5), the impedance model $\mathbf{Z}$ can be obtained. From the above analysis, unified modeling procedure can be summarized by the following:

1) Establish the functional relationship between $\Delta\theta$ and its input as shown in (4);
2) Substitute (4) into (3) to get the relationship between vectors under two frames as shown in (5);
3) Develop the control block diagram according to (5);
4) Calculate the converter's impedance model according to control block diagram.

A. IMPEDANCE MODEL OF GRID-FORMING CONVERTER

Fig. 3 shows a typical configuration of a grid-forming converter [11]. For different types of grid-forming converters, such as VSG and SPC, only the power loop in Fig. 3(a) is replaced by the corresponding power-based synchronization, while the inner loop remains the same [11], [24], [25].

For better establishing the grid-forming converter's model, droop control is chosen as an example. Under this circumstance, $\Delta\theta$ is related to the variation of active power, which is

$$\Delta\theta = m_p \Delta P \tag{6}$$

where m_p represents proportional coefficient between active power and phase angle, which satisfies equation below.

$$m_p = -\frac{n_p \omega_f}{s(s+\omega_f)} \tag{7}$$

where n_p represents droop control coefficient of active power, ω_f represents cut-off frequency of a first-order low-pass filter.

The active power is associate with voltage and current, which is

$$\Delta P = \frac{3}{2} \begin{bmatrix} I_d^c & I_q^c \end{bmatrix} \begin{bmatrix} \Delta v_{cd}^c \\ \Delta v_{cq}^c \end{bmatrix} + \frac{3}{2} \begin{bmatrix} V_{cd}^c & V_{cq}^c \end{bmatrix} \begin{bmatrix} \Delta i_d^c \\ \Delta i_q^c \end{bmatrix} \tag{8}$$

Substitute (6) and (8) to (3),

$$\begin{bmatrix} \Delta v_{cd}^c \\ \Delta v_{cq}^c \end{bmatrix} = \begin{bmatrix} \Delta v_{cd}^s \\ \Delta v_{cq}^s \end{bmatrix} + \mathbf{G}_1' \begin{bmatrix} \Delta v_{cd}^c \\ \Delta v_{cq}^c \end{bmatrix} + \mathbf{G}_2' \begin{bmatrix} \Delta i_d^c \\ \Delta i_q^c \end{bmatrix} \tag{9}$$

Similarly,

$$\begin{bmatrix} \Delta i_d^c \\ \Delta i_q^c \end{bmatrix} = \begin{bmatrix} \Delta i_d^s \\ \Delta i_q^s \end{bmatrix} + \mathbf{G}_3' \begin{bmatrix} \Delta v_{cd}^c \\ \Delta v_{cq}^c \end{bmatrix} + \mathbf{G}_4' \begin{bmatrix} \Delta i_d^c \\ \Delta i_q^c \end{bmatrix} \tag{10}$$

Combine (9) and (10)

$$\begin{bmatrix} \Delta v_{cd}^c \\ \Delta v_{cq}^c \end{bmatrix} = \mathbf{G_1} \begin{bmatrix} \Delta v_{cd}^s \\ \Delta v_{cq}^s \end{bmatrix} + \mathbf{G_2} \begin{bmatrix} \Delta i_d^s \\ \Delta i_q^s \end{bmatrix} \tag{11}$$

$$\begin{bmatrix} \Delta i_d^c \\ \Delta i_q^c \end{bmatrix} = \mathbf{G}_3 \begin{bmatrix} \Delta v_{cd}^s \\ \Delta v_{cq}^s \end{bmatrix} + \mathbf{G}_4 \begin{bmatrix} \Delta i_d^s \\ \Delta i_q^s \end{bmatrix} \tag{12}$$

Similarly,

$$\begin{bmatrix} \Delta i_{Ld}^c \\ \Delta i_{Lq}^c \end{bmatrix} = \begin{bmatrix} \Delta i_{Ld}^s \\ \Delta i_{Lq}^s \end{bmatrix} + \mathbf{G_5} \begin{bmatrix} \Delta v_{cd}^s \\ \Delta v_{cq}^s \end{bmatrix} + \mathbf{G_6} \begin{bmatrix} \Delta i_d^s \\ \Delta i_q^s \end{bmatrix} \tag{13}$$

$$\begin{bmatrix} \Delta v_{rd}^c \\ \Delta v_{rq}^c \end{bmatrix} = \begin{bmatrix} \Delta v_{rd}^s \\ \Delta v_{rq}^s \end{bmatrix} + \mathbf{G_7} \begin{bmatrix} \Delta v_{cd}^s \\ \Delta v_{cq}^s \end{bmatrix} + \mathbf{G_8} \begin{bmatrix} \Delta i_d^s \\ \Delta i_q^s \end{bmatrix} \tag{14}$$

The detailed expressions of $\mathbf{G_1'}$ and $\mathbf{G_2'}$ and $\mathbf{G_i}$ (i=12……,8) are shown in the Appendix.

The reactive power loop mainly affects the d-axis reference voltage, and the q-axis reference voltage is directly set to 0. The relationship between reactive power and d-axis reference voltage is

$$\Delta v_{dref} = m_q \Delta Q \tag{15}$$

where m_q represents the proportional coefficient between the d-axis voltage reference value and the reactive power, and the expression is

$$m_q = -\frac{n_q \omega_f}{s + \omega_f} \tag{16}$$

where n_q represents the droop control coefficient of reactive power. The perturbation of reactive power is also determined by the perturbations of voltage and current, which is

$$\Delta Q = \frac{3}{2} \begin{bmatrix} -I_q^c & I_d^c \end{bmatrix} \begin{bmatrix} \Delta v_{cd}^c \\ \Delta v_{cq}^c \end{bmatrix} + \frac{3}{2} \begin{bmatrix} V_{cq}^c & -V_{cd}^c \end{bmatrix} \begin{bmatrix} \Delta i_d^c \\ \Delta i_q^c \end{bmatrix} \tag{17}$$

Thus

$$\begin{bmatrix} \Delta v_{dref} \\ 0 \end{bmatrix} = \begin{bmatrix} m_q \Delta Q \\ 0 \end{bmatrix} = \mathbf{G_{mq}} \mathbf{G_Q^v} \begin{bmatrix} \Delta v_{cd}^c \\ \Delta v_{cq}^c \end{bmatrix} + \mathbf{G_{mq}} \mathbf{G_Q^i} \begin{bmatrix} \Delta i_d^c \\ \Delta i_q^c \end{bmatrix} \tag{18}$$

where $\mathbf{G_Q^v}$ represents the transfer function matrix between voltage and reactive power, $\mathbf{G_Q^i}$ represents the transfer function matrix between current and reactive power, $\mathbf{G_{mq}}$ represents the reactive power coefficient transfer function matrix.

According to the above analysis, the model of the grid-forming converter is developed in Fig. 4. $\mathbf{G_{PI}^v}$ represents PI controller in voltage loop. $\mathbf{G_{PI}^i}$ represents PI controller in current loop, and $\mathbf{Y_C}$ represents capacitor branch. $\mathbf{G_{del}}$ represents delay matrixes. All the above-mentioned matrixes are shown in the Appendix with details.

According to Fig. 4, the impedance model of the grid-forming converter is

$$\begin{aligned} \mathbf{Z} = \Big\{ \Big[& \left(\mathbf{Y_L G_{del} G_{PI}^i G_{PI}^v}\right) \left(\mathbf{G_{mq} G_Q^v G_1} + \mathbf{G_{mq} G_Q^i G_3} - \mathbf{G_1}\right) \\ & - \left(\mathbf{Y_L G_{del} G_{PI}^i G_5} + \mathbf{Y_L G_7} + \mathbf{Y_L}\right) \Big] \\ & - \left(\mathbf{E} + \mathbf{Y_L G_{del} G_{PI}^i}\right) \mathbf{Y_c} \Big\}^{-1} \Big\{ \left(\mathbf{E} + \mathbf{Y_L G_{del} G_{PI}^i}\right) \\ & - \Big[\left(\mathbf{Y_L G_{del} G_{PI}^i G_{PI}^v}\right) \left(\mathbf{G_{mq} G_Q^v G_2} + \mathbf{G_{mq} G_Q^i G_4} - \mathbf{G_2}\right) \\ & - \left(\mathbf{Y_L G_{del} G_{PI}^i G_6} + \mathbf{Y_L G_8}\right) \Big] \Big\} \end{aligned} \tag{19}$$

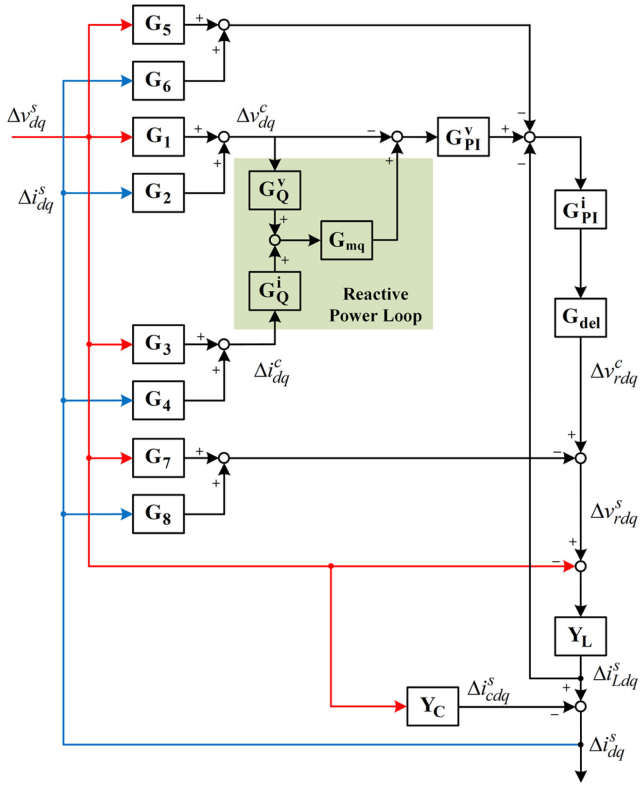

FIGURE 4. Model of the grid-forming converter.

For other types of grid-forming converters, namely converters adopting other control strategies, if the inner control loop (e.g., voltage/current loop) and main circuit are same except for the active power loop, the impedance model can directly adopt (19), and only change m_p in (6). Taking VSG as an example, droop control is equivalent to VSG if their parameters satisfy (20) and (21) [26]:

$$\frac{1}{J} = \omega_g \omega_f n_p \tag{20}$$

$$D_q = \frac{1}{\omega_g n_p} \tag{21}$$

where J is inertia of generator, D_q is the damping coefficient, ω_g is the synchronous angular frequency.

For the SPC, it uses the gain k and cut-off frequency ω_c to obtain phase angle. The transfer function of PLC is [25]

$$G_{PLC} = k \frac{\omega_c}{s + \omega_c} \tag{22}$$

If k and ω_c fulfill the following requirements

$$\omega_c = \frac{1}{D_q \omega_g} \tag{23}$$

$$k = \frac{2D_q}{J} \tag{24}$$

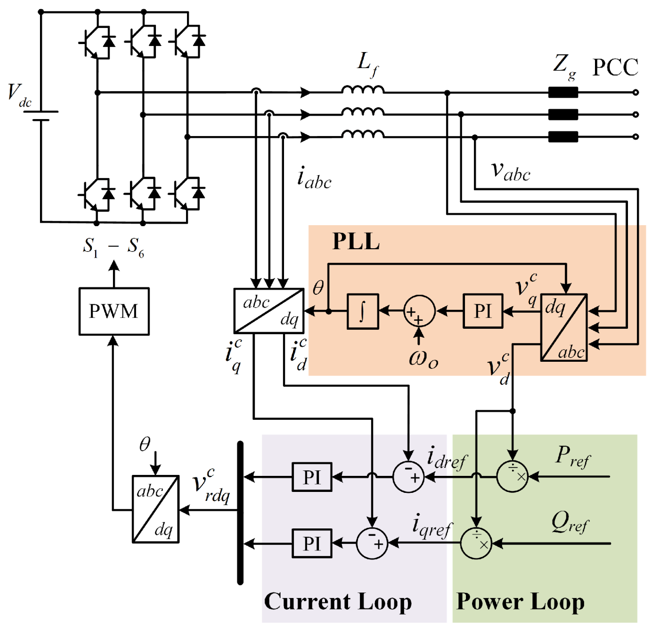

FIGURE 5. Configuration of the grid-following converter.

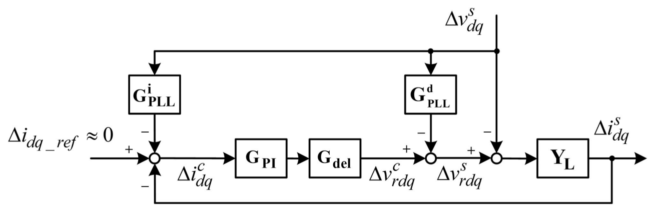

FIGURE 6. Model of the grid-following converter.

the transfer function of PLC is same to that of VSG.

$$G_{PLC} = \frac{1}{\omega_g(Js + D_q)} \tag{25}$$

To sum up, when parameters of droop control, VSG and SPC satisfy (20), (21), (23) and (24), these three strategies can be equivalent and have same impedance model.

B. IMPEDANCE MODEL OF GRID-FOLLOWING CONVERTER

The typical structure of grid-following converter is shown in Fig. 5 [4]. Its block diagram is mainly composed of three parts: power loop, current loop and PLL. Since the bandwidth of the power loop usually is low, its influence can be ignored in modeling, and only the current loop and PLL are considered. For grid-following converter, $\Delta\theta$ is related to the q-axis voltage [4]–[6], which is

$$\Delta\theta = G_{PLL}\Delta v_q^s \tag{26}$$

where G_{PLL} is PLL closed-loop transfer function. Similar to grid-forming converter, and using (10), (11), and (13), its impedance model can be obtained and shown in Fig. 6.

The transfer function matrices of the block diagram are shown in the Appendix. Based on Fig. 6, the impedance

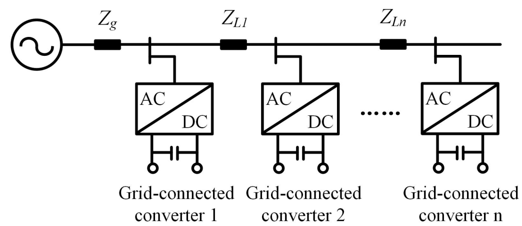

FIGURE 7. Configuration of a radial grid.

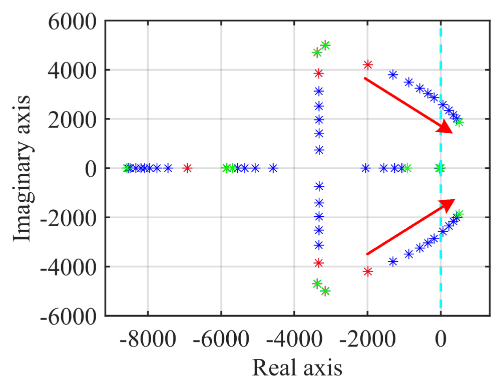

FIGURE 8. Root locus of the system by reduction of SCR (Bus 1 and bus 2 are grid-following converters).

model is

$$\mathbf{Z} = (\mathbf{Y_L} + \mathbf{Y_L G_{PLL}^d} + \mathbf{Y_L G_{del} G_{PI} G_{PLL}^i})^{-1} \times (\mathbf{E_{2\times 2}} + \mathbf{Y_L G_{del} G_{PI}}) \tag{27}$$

IV. STABILITY AND SENSITIVITY ANALYSIS

A. STABILITY OF A RADIAL GRID

The configuration of a radial grid with power converters is shown in Fig. 7, where Z_g is the grid impedance and Z_L is the line impedance. N converters are connected to different buses. For better analyzing system stability, a two-bus system with two converters is used as an example in the followings. The influences of different parameters on the stability can be extended to the N-bus system.

In case 1, grid-following converters are connected to bus 1 and bus 2. Root locus of the system with the change of SCR is shown in Fig. 8. By reduction of SCR, the system becomes unstable. This indicates that the grid-following converter is suitable for the strong grid. The system can become more stable when the grid is stronger. Similar to SCR, by increase of the line impedance, the system becomes unstable. For better understanding the effect of line impedance, the relationship between R/X ratio and stability margin is shown in Fig. 9. In this paper, the stability margin is defined as

$$\text{margin} = \frac{\sigma}{\sigma_B} \tag{28}$$

where σ is the real part of pole, σ_B is the nominal value of the stability margin. A higher margin indicates a more stable system. As shown in Fig. 9, by increasing of R/X ratio, the

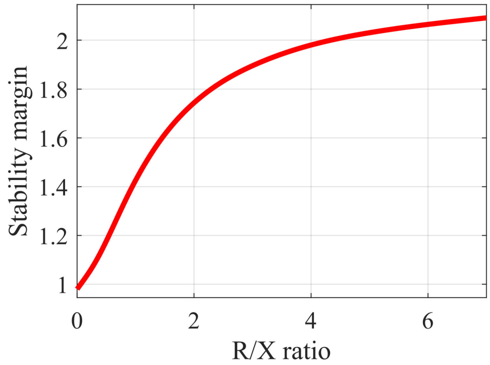

FIGURE 9. The relationship between R/X ratio and stability margin (Bus 1 and bus 2 are grid-following converters).

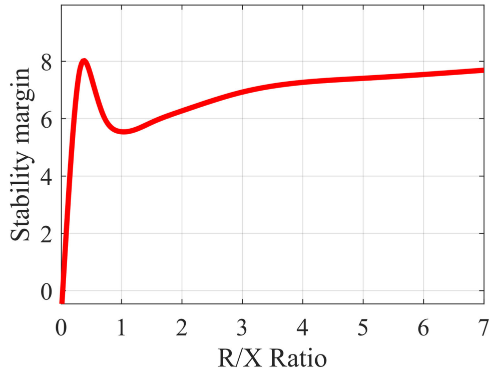

FIGURE 11. The relationship between R/X ratio and stability margin (Bus 1 and bus 2 are grid-forming converters).

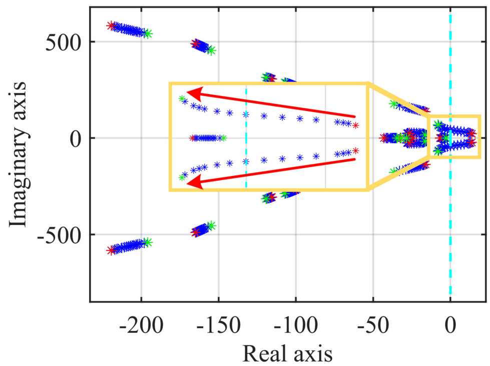

FIGURE 10. Root locus of the system by reduction of SCR (Bus 1 and bus 2 are grid-forming converters).

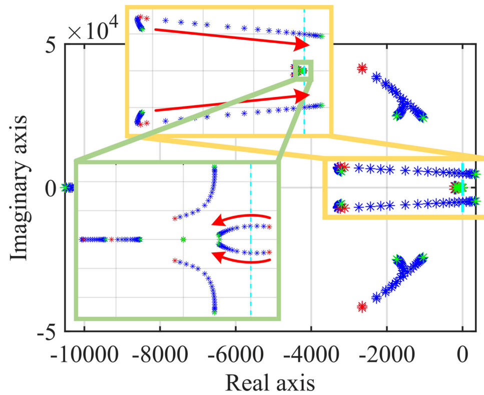

FIGURE 12. Root locus of the system by reduction of SCR (Bus 1 is grid-following converter and bus 2 is grid-forming converter).

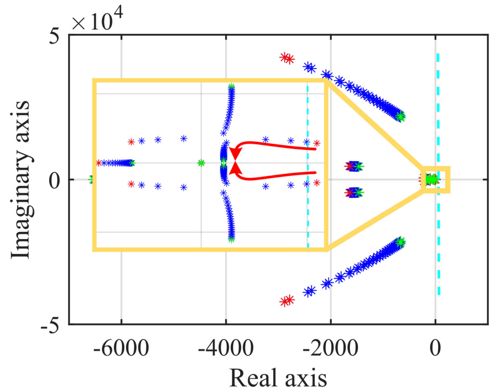

FIGURE 13. Root locus of the system by increase of the line impedance (Bus 1 is grid-following converter and Bus 2 is grid-forming converter, SCR=4.4).

stability margin increases, which indicates this system is more stable when the network is resistive.

In case 2, grid-forming converters are connected to bus 1 and bus 2. Root locus of the system with the change of SCR is shown in Fig. 10. By reduction of SCR, the system becomes stable. This indicates that the grid-forming converter is suitable for the weak grid. The system can become more stable when the grid is weaker. Similar to SCR, by increase of the line impedance, the system becomes stable. The relationship between R/X ratio and stability margin is shown in Fig. 11. When R/X ratio is smaller than 1, stability margin reaches its peak when R/X ratio equals to 0.3.

In case 3, the grid-following converter is connected to bus 1and the grid-forming converter is connected to bus 2. Root locus of the system with the change of SCR is shown in Fig. 12. By reduction of SCR, the system becomes more stable in the very beginning and if SCR continues to decrease, the system becomes unstable. The stable range of SCR is 1 to 4.4. This is because with the increasing of SCR, the participation factor of the grid-forming converter increases and it starts to support the voltage. When SCR is too low, the effect of the grid-following converter becomes dominant which leads to the instability. Root locus of the system with the change of the line impedance under different grid condition is shown in Figs. 13 and 14. When the grid is strong, by increase of the line impedance, the system becomes stable. This is because when SCR is high, the effect of the grid-forming converter becomes dominant which leads to the instability. By increase of the line impedance, the grid becomes weaker, which is beneficial for the stability of grid-forming converter. When

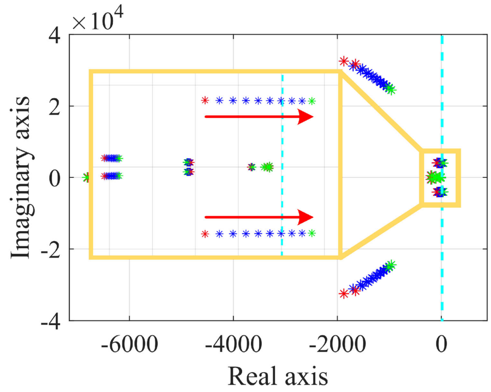

FIGURE 14. Root locus of the system by increase of the line impedance (Bus 1 is grid-following converter and Bus 2 is grid-forming converter, SCR=2.2).

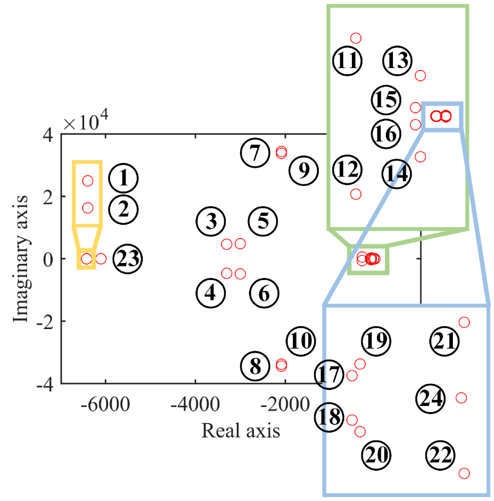

FIGURE 15. The location of closed-loop poles.

TABLE 1. SCR Range for Four Cases

	Bus 1	Bus 2	SCR range
Case 1	Grid-following	Grid-following	>5
Case 2	Grid-forming	Grid-forming	<3
Case 3	Grid-following	Grid-forming	1-4.4
Case 4	Grid-forming	Grid-following	1.5-2.8

the grid is weak, by increase of the line impedance, the system becomes unstable. This is because grid-forming converter can be equivalent to a voltage source that supplies power to the grid-following converter together with the grid. If the line impedance is too large, the grid-forming converter can no longer supply the system and the effect of the grid-following converter becomes dominant.

In case 4, the grid-forming converter is connected to bus 1and the grid-following converter is connected to bus 2. The case is similar to case 3: system is stable within a range of SCR and by increase of the line impedance, the system becomes unstable under weak grid. However, the stable range of case 4 is 1.5 to 2.8, which is smaller than that of case 3.

From the above analysis, Table 1 is obtained. The first two cases are suitable for very specific cases. The third and fourth ones are more adaptive to the general grid. In particular, the stable range of the third case is larger than that of the forth one. In the following studies, the third case will be further studied in terms of sensitivity analysis.

B. PARAMETER SENSITIVITY ANALYSIS

Parameter sensitivity analysis investigates the effects of parameter variations on the closed-loop poles of the system. Among all the control parameters, the effects of the following four parameters are considered in this analysis, namely the virtual inertia J, the virtual damping factor D_p, the proportional gain of the PLL k_{pPLL}, the integral gain of the PLL k_{iPLL}. Three cases with different SCR have been studied, namely, SCR=10, SCR=5, SCR=2.5. The location of the closed-loop poles of the system is shown in Fig. 15.

The parameter sensitivity is defined in (29):

$$\frac{\partial \sigma}{\partial Y} = \frac{\sigma|_{Y_o} - \sigma|_{Y_\Delta}}{\sigma|_{Y_o}} \tag{29}$$

where σ is the real part of pole, $Y = \{J, D_p, k_{ppll}, k_{ipll}\}$, $\sigma|_{Y_o}$ is the value of σ calculated for Y_o, whereas $\sigma|_{Y_\Delta}$ is the value of σ when Y_o has been increased of a small quantity Δ. In general, a bar with positive value indicates a more stable condition (i.e., pole moves leftwards) when increasing the related parameters, whereas a negative bar indicates a less stable condition (pole moves rightwards). The parameter sensitivity under three cases is shown in Fig. 16.

For all the case studies, the poles λ_{17}, λ_{18}, λ_{21} to λ_{24} are relatively sensitive to the variation of selected parameters. These poles are the closed-loop dominant poles. By increase of D_p, k_{pPLL} and k_{iPLL}, these parameters have a negative impact on system stability. By increase of J, it has a positive impact on system stability. For a SCR of 10, all the other poles seem to be almost insensitive to the parameter variations except λ_5 and $\lambda_{6.}$ Moreover, the lower the SCR, the more sensitive of the poles λ_5 to λ_{10} to the variations of k_{pPLL}, which are moving leftwards. However, λ_5 to λ_{10} are far away from imaginary axis and the change of these poles will not cause system instability, which means the change of SCR has little impact on the stability of system when hybrid types of converters are used.

The above research investigates the influence of SCR and line impedance under four cases and analyzes parameter sensitivity, which provides a guideline for system design to avoid instability problems:

1) Grid-following converters are preferred to strong grid while grid-forming converters can be connected to weak grid. If both types of converters are utilized, it is suggested to have grid-following converters being closer to the substation and grid-forming converters being farther away from it;

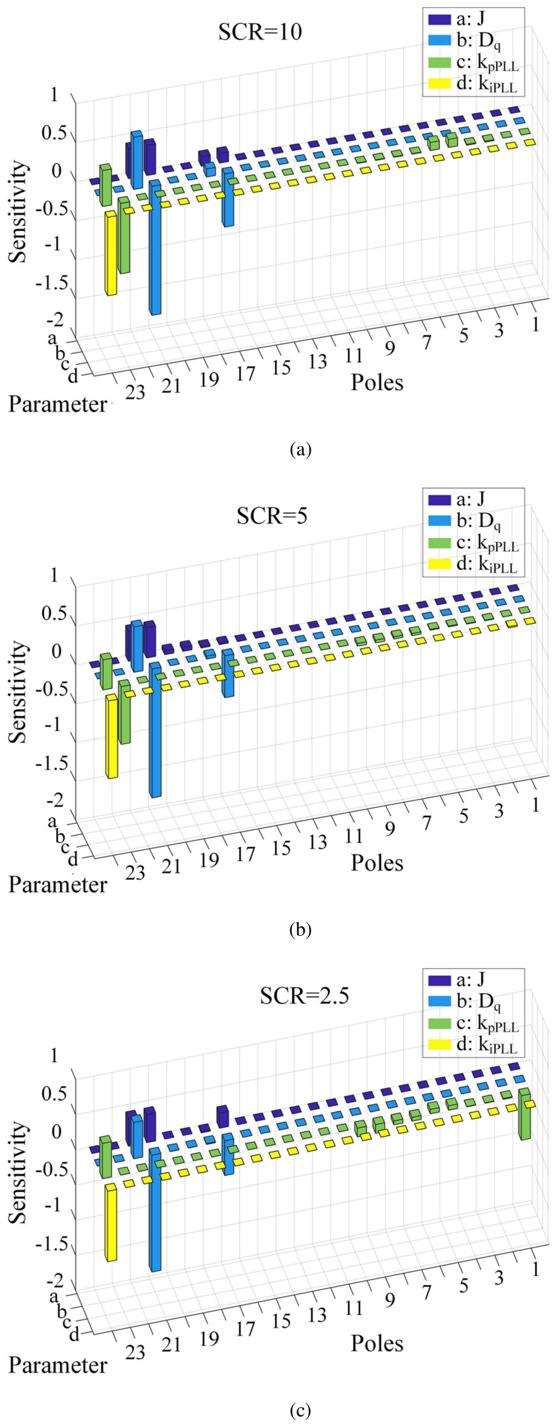

FIGURE 16. Parameter sensitivity under different SCR: (a) SCR=5, (b) SCR=5, (c) SCR=2.5.

2) For the grid-following converters, a network with resistive cable should be chosen. Nevertheless, for the grid-forming converters, the inductive cable would be recommended;
3) The decrease of PLL bandwidths as well D_q and the increase of J make system more stable.

TABLE 2. Converter Parameters

	Symbol	Definition	Value
General parameters	U_{dc}	DC voltage	650V
	L_f	Filter inductance	3mH
Grid-following converter	k_{ppll}	PLL proportional gain	18.4
	k_{ipll}	PLL integral gain	169.3
	k_p	proportional gain	16
	k_i	integral gain	600
Grid-forming converter	k_{pi}	Current loop proportional gain	1
	k_{ii}	Current loop integral gain	500
	k_{pv}	Voltage loop proportional gain	0.05
	k_{iv}	Voltage loop integral gain	250
	C_f	Filter capacitor	1.5μF
	R_C	Resistance	2Ω
	J	Current loop proportional gain	0.4935
	D_q	Active power droop coefficient	63
	n_q	Reactive power coefficient	1e-4

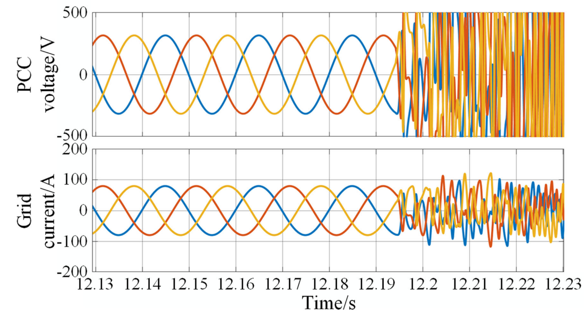

FIGURE 17. Voltage and current waves by reduction of SCR (Case 1).

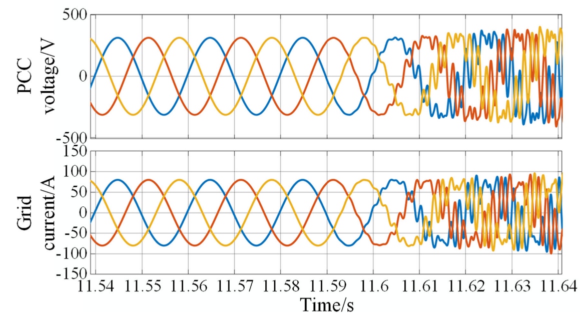

FIGURE 18. Voltage and current waves by increase of line impedance (Case 1).

V. SIMULATION AND EXPERIMENTAL VALIDATION

A. SIMULATION

In order to verify the correctness of the previous analysis, simulations are carried out in the MATLAB/Simulink with the aid of PLECS toolbox. Parameters are shown in Table 2.

In case 1, the influence of SCR and line impedance in shown in Figs. 17 and 18. By reduction of SCR from 4.4 to 0.8, the system becomes unstable, indicating that the decrease of SCR will lead to instability. By increase of line impedance from 0.05 p.u. to 0.26 p.u, the system becomes unstable. It shows that the increase of SCR and the decrease of the line impedance is beneficial for system stability.

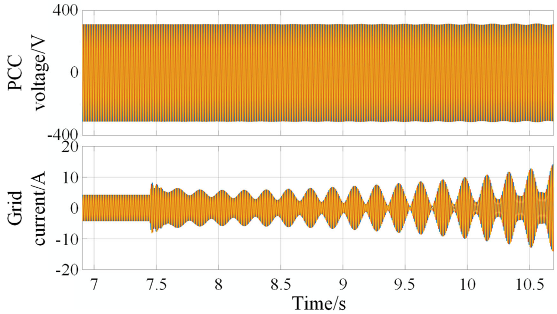

FIGURE 19. Voltage and current waves by increase of SCR (Case 2).

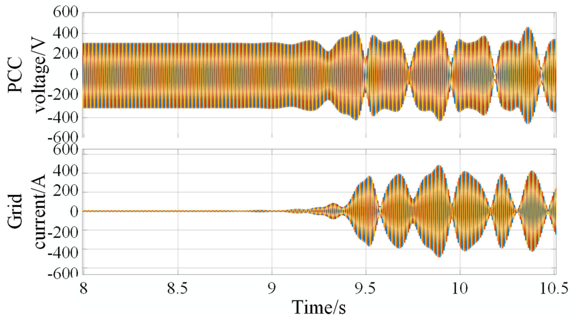

FIGURE 20. Voltage and current waves by reduction of the line impedance (Case 2).

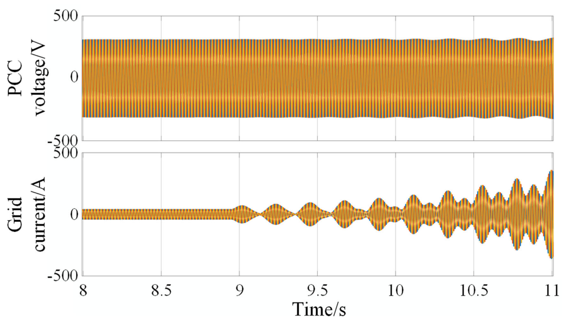

FIGURE 21. Voltage and current waves by increase of SCR (Case 3).

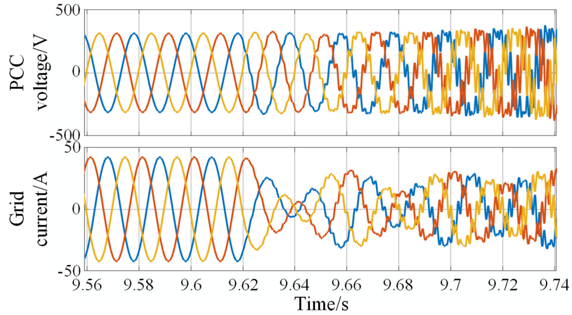

FIGURE 22. Voltage and current waves by reduction of SCR (Case 3).

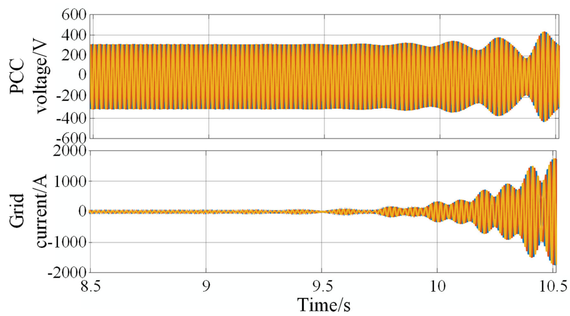

FIGURE 23. Voltage and current waves by reduction of the line impedance (Case 3, strong grid).

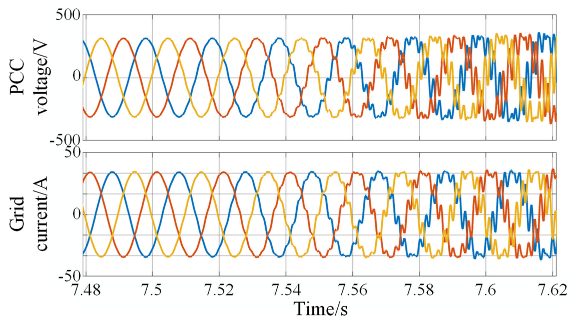

FIGURE 24. Voltage and current waves by increase of the line impedance (Case 3, weak grid).

In case 2, the influence of SCR and line impedance in shown in Figs. 19 and 20. In this case, the phenomenon is completely opposite to the previous one. The increase of SCR and the decrease of line impedance leads to system instability.

In case 3, the influence of SCR and line impedance in shown in Figs. 21–24. By increase of SCR from 4.4 to 13, the system becomes unstable. By decrease of SCR from 2.2 to 0.3, the system becomes unstable. It shows that this system is suitable for general grid. By decrease of the line decreases from 0.82 p.u. to 0.08 p.u., the system becomes unstable under the strong grid. By increase of the line impedance from 0.82 p.u. to 6.6 p.u., the system becomes unstable under the weak grid. The influence of the line impedance varies with the grid condition.

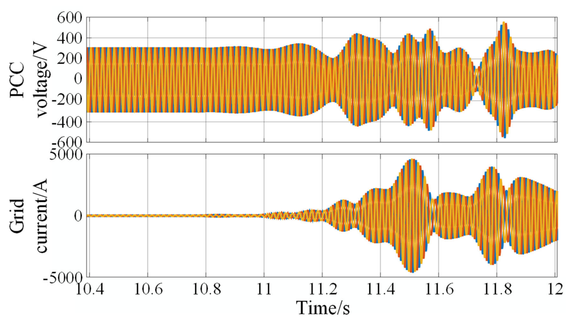

FIGURE 25. Voltage and current waves by increase of SCR (Case 4).

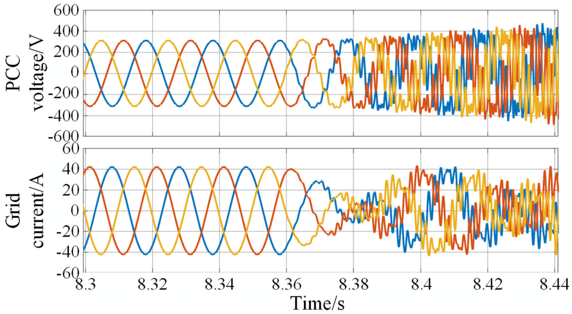

FIGURE 26. **Voltage and current waves by reduction of SCR (Case 4).**

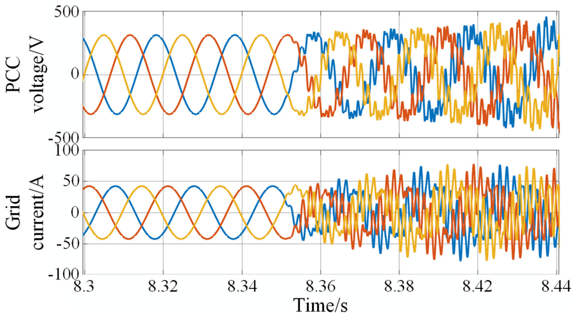

FIGURE 27. **Voltage and current waves by increase of the line impedance (Case 4, weak grid).**

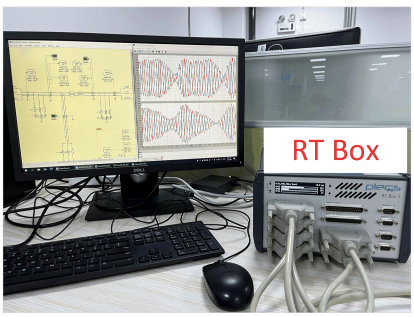

FIGURE 28. **HiL tests setup.**

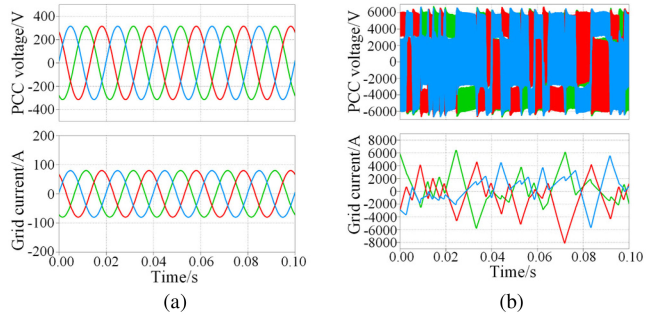

FIGURE 29. **PCC voltage and grid current waveforms by reduction of SCR (Case 1): (a) stable (SCR=4.4), (b) unstable (SCR=0.77).**

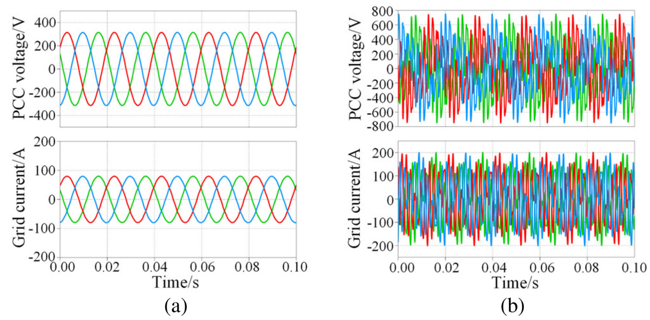

FIGURE 30. **PCC voltage and grid current waveforms by increase of the line impedance (Case 1): (a) stable (Line impedance is 0.05 p.u.), (b) unstable (Line impedance is 0.26 p.u.).**

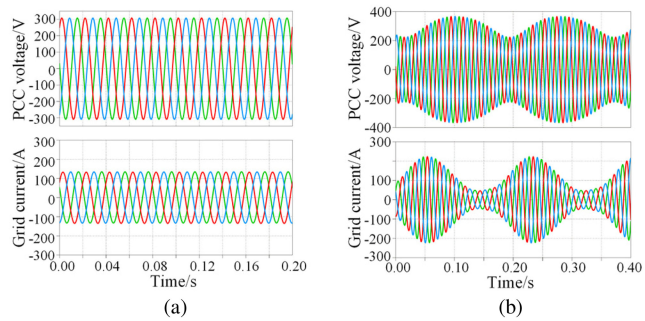

FIGURE 31. **PCC voltage and grid current waveforms by increase of SCR (Case 2): (a) stable (SCR=0.46), (b) unstable (SCR= 0.76).**

In case 4, the influence of SCR and line impedance is in shown in Figs. 25–27. In this case, the phenomenon is similar to case 3. The system is unstable if grid is too strong or too weak. And under weak grid, the increase of the line impedance leads to system instability.

B. HARDWARE-IN-THE-LOOP VALIDATIONS

In order to validate previous analysis, HiL tests with the aid of RT Box have been done. The setup of HiL tests is shown in Fig. 28.

In case 1, the PCC voltage and grid current waveforms by reduction of SCR and by increase of the line impedance are shown in Figs. 29 and 30. The reduction of SCR and increase of line impedance will cause system instability.

In case 2, the PCC voltage and grid current waveforms by increase of SCR and by reduction of line impedance are shown in Figs. 31 and 32. The increase of SCR and reduction of line impedance will cause system instability.

In case 3, the PCC voltage and grid current waveforms by reduction of SCR are shown in Fig. 33(a) and Fig. 33(b). At this time, the system changes from unstable to stable. If SCR continues to decrease, the PCC voltage and grid current waveforms are shown in Fig. 33(c) and the system becomes unstable. In the same situation, the PCC voltage and grid current waveforms by decrease of the line impedance under strong grid and weak grid are shown in Fig. 34.

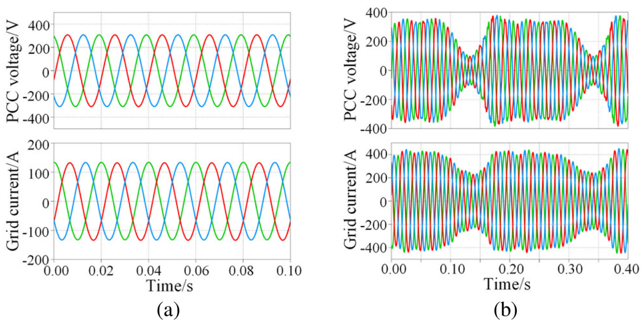

FIGURE 32. PCC voltage and grid current waveforms by decrease of the line impedance (Case 2): (a) stable (Line impedance is 1.03 p.u.), (b) unstable (Line impedance is 0.51 p.u.).

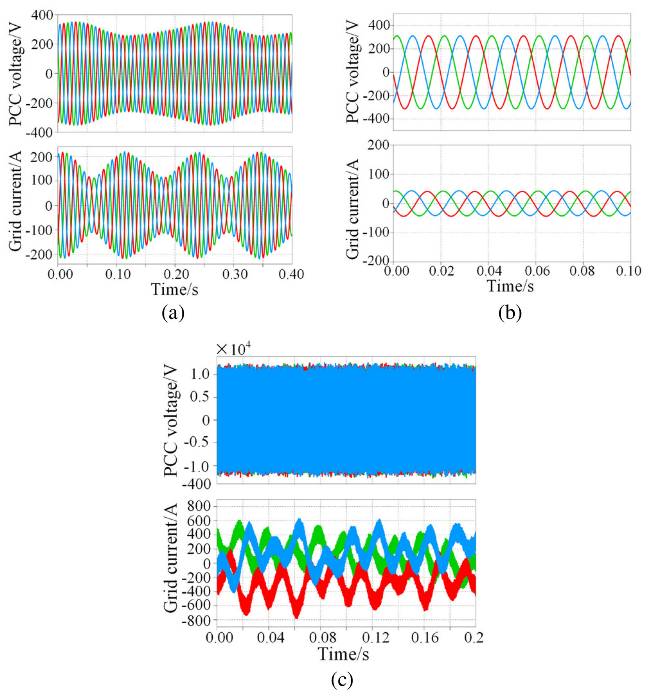

FIGURE 33. PCC voltage and grid current waveforms by reduction of SCR (Case 3): (a) unstable (SCR=13.77), (b) stable (SCR=4.4), (c) unstable (SCR=0.46).

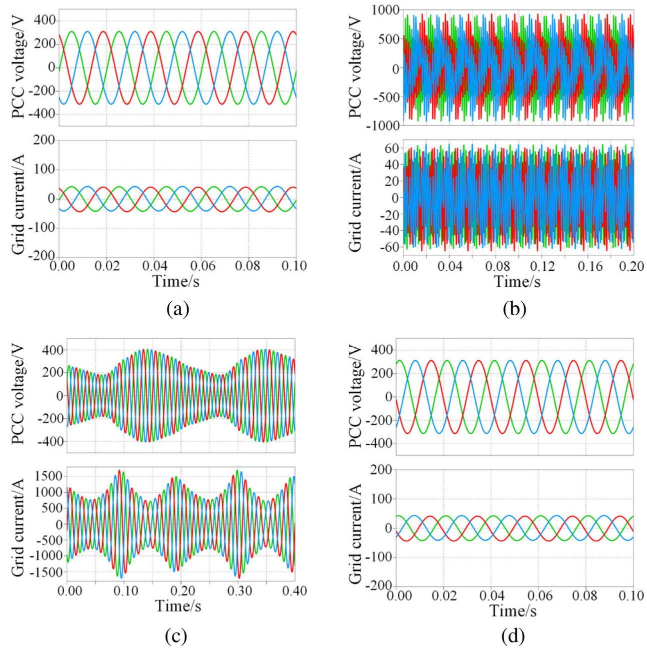

FIGURE 34. PCC voltage and grid current waveforms by increase of the line impedance (Case 3): (a) stable (Weak grid, line impedance=0.26 p.u.), (b) unstable (Weak grid, line impedance=1.02 p.u.), (c) unstable (Strong grid, line impedance=0.05 p.u.), (d) stable (Strong grid, line impedance=0.26 p.u.).

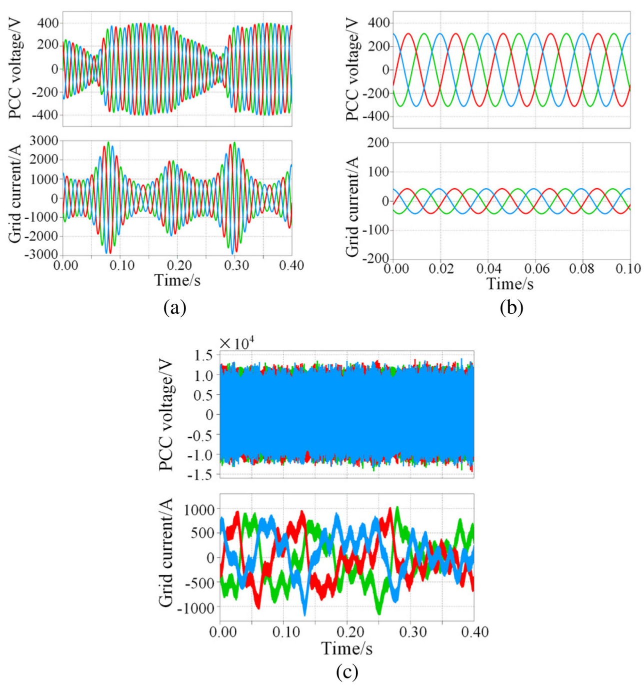

FIGURE 35. PCC voltage and grid current waveforms by reduction of SCR (Case 4): (a) unstable (SCR=4.4), (b) stable (SCR=2.2), (c) unstable (SCR=0.57).

In case 4, the phenomenon is similar to case 3. The system is stable within a range of SCR, which is shown in Fig. 35. And under strong grid, system becomes unstable by increase of line impedance. Different from case 3, case 4 is difficult to be stable in strong grid.

VI. CONCLUSION

This paper proposes unified modeling procedure and applies it to two types of converters. Based on the impedance models, the stability of a radial grid with power converters under four different cases are discussed. Particularly, the influence of SCR and line impedance are considered. It indicates that the system with both grid-forming and grid-following converters are the optimal solution. Moreover, a comprehensive parameter sensitivity analysis is performed. It shows the increase of J has a positive impact on system stability and the increase of

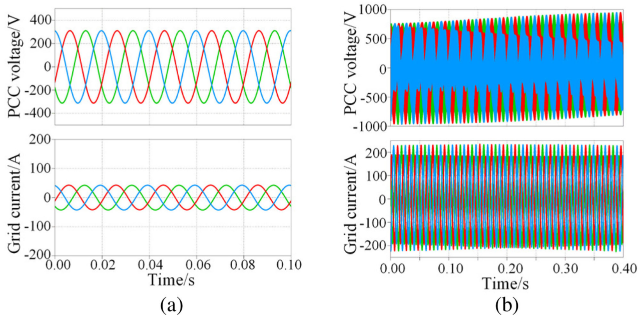

FIGURE 36. PCC voltage and grid current waveforms by increase of the line impedance (Case 4): (a) stable (weak grid, line impedance=0.26 p.u.), (b) unstable (weak grid, line impedance=1.02 p.u.).

D_p, k_{pPLL} and k_{iPLL} has a negative impact on system stability. The change of SCR has little impact on system stability when both grid-forming and grid-following converters being connected to the grid. Simulations and HiL results are provided to verify the effectiveness of the analysis.

APPENDIX

$$\mathbf{G}_1' = a\begin{bmatrix} -I_d^c V_{cq}^s & -I_q^c V_{cq}^s \\ I_d^c V_{cd}^s & I_q^c V_{cd}^s \end{bmatrix} \mathbf{G}_2' = a\begin{bmatrix} -V_{cd}^c V_{cq}^s & -V_{cq}^c V_{cq}^s \\ V_{cd}^c V_{cd}^s & V_{cq}^c V_{cd}^s \end{bmatrix}$$

$$\mathbf{G}_3' = a\begin{bmatrix} -I_d^c I_{oq}^s & -I_q^c I_{oq}^s \\ I_d^c I_{od}^s & I_q^c I_{od}^s \end{bmatrix} \mathbf{G}_4' = a\begin{bmatrix} -I_q^s V_{cd}^c & -I_q^s V_{cq}^c \\ I_d^s V_{cd}^c & I_d^s V_{cq}^c \end{bmatrix}$$

$$\mathbf{G_1} = \begin{bmatrix} 1 - aV_{cq}^s I_d^s & -aV_{cq}^s I_q^s \\ aV_{cd}^s I_d^s & 1 + aV_{cd}^s I_q^s \end{bmatrix} \mathbf{G_2} = \begin{bmatrix} -aV_{cq}^s V_{cd}^s & -aV_{cq}^s V_{cq}^s \\ aV_{cd}^s V_{cd}^s & aV_{cd}^s V_{cq}^s \end{bmatrix}$$

$$\mathbf{G_3} = \begin{bmatrix} -aI_d^s I_q^s & -aI_q^s I_q^s \\ aI_d^s I_d^s & aI_d^s I_q^s \end{bmatrix} \mathbf{G_4} = \begin{bmatrix} 1 - aV_{cd}^s I_q^s & -aV_{cq}^s I_q^s \\ aV_{cd}^s I_d^s & 1 + aV_{cq}^s I_d^s \end{bmatrix}$$

$$\mathbf{G_5} = \begin{bmatrix} -aI_d^s I_{Lq}^s & -aI_q^s I_{Lq}^s \\ aI_d^s I_{Ld}^s & aI_q^s I_{Ld}^s \end{bmatrix} \mathbf{G_6} = \begin{bmatrix} -aV_{cd}^s I_{Lq}^s & -aV_{cq}^s I_{Lq}^s \\ aV_{cd}^s I_{Ld}^s & aV_{cq}^s I_{Ld}^s \end{bmatrix}$$

$$\mathbf{G_7} = \begin{bmatrix} -aI_d^s V_{rq}^s & -aI_q^s V_{rq}^s \\ aI_d^s V_{rd}^s & aI_q^s V_{rd}^s \end{bmatrix} \mathbf{G_8} = \begin{bmatrix} -aV_{cd}^s V_{rq}^s & -aV_{cq}^s V_{rq}^s \\ aV_{cd}^s V_{rd}^s & aV_{cq}^s V_{rd}^s \end{bmatrix}$$

where

$$a = -\frac{3}{2} m_p$$

$$\mathbf{G_Q^v} = \frac{3}{2}\begin{bmatrix} -I_q^c & I_d^c \\ 0 & 0 \end{bmatrix} \mathbf{G_Q^i} = \frac{3}{2}\begin{bmatrix} V_{cq}^c & -V_{cd}^c \\ 0 & 0 \end{bmatrix}$$

$$\mathbf{G_{nq}} = \begin{bmatrix} -n_q & 0 \\ 0 & -n_q \end{bmatrix} \mathbf{G_{LPF}} = \begin{bmatrix} \frac{\omega_f}{s+\omega_f} & 0 \\ 0 & \frac{\omega_f}{s+\omega_f} \end{bmatrix}$$

$$\mathbf{G_{PI}^v} = \begin{bmatrix} k_{pv} + \frac{k_{iv}}{s} & 0 \\ 0 & k_{pv} + \frac{k_{iv}}{s} \end{bmatrix} \mathbf{G_{PI}^i} = \begin{bmatrix} k_{pi} + \frac{k_{ii}}{s} & 0 \\ 0 & k_{pi} + \frac{k_{ii}}{s} \end{bmatrix}$$

$$\mathbf{Y_C} = \mathbf{Z_C^{-1}} = \begin{bmatrix} R_c + \frac{s}{(s^2+\omega^2)C} & \frac{\omega}{(s^2+\omega^2)C} \\ -\frac{\omega}{(s^2+\omega^2)C} & R_c + \frac{s}{(s^2+\omega^2)C} \end{bmatrix}^{-1}$$

$$\mathbf{G_{PLL}^v} = \begin{bmatrix} 1 & V_q^s G_{PLL} \\ 0 & 1 - V_d^s G_{PLL} \end{bmatrix} \mathbf{G_{PLL}^i} = \begin{bmatrix} 0 & G_{PLL} I_q^s \\ 0 & -G_{PLL} I_d^s \end{bmatrix}$$

$$\mathbf{G_{PLL}^d} = \begin{bmatrix} 0 & G_{PLL} V_{rq}^s \\ 0 & -G_{PLL} V_{rd}^s \end{bmatrix} \mathbf{G_{PI}} = \begin{bmatrix} k_p + \frac{k_i}{s} & 0 \\ 0 & k_p + \frac{k_i}{s} \end{bmatrix}$$

$$\mathbf{G_{del}} = \begin{bmatrix} \frac{1}{1+1.5T_s s} & 0 \\ 0 & \frac{1}{1+1.5T_s s} \end{bmatrix} \mathbf{Y_L} = \frac{1}{L(s^2+\omega^2)}\begin{bmatrix} s & \omega \\ -\omega & s \end{bmatrix}$$

REFERENCES

[1] X. Xie, J. He, H. Mao, and H. Li, "New issues and classification of power system stability with high shares of renewables and power electronics," *Proc. CSEE*, vol. 41, no. 2, pp. 461–475, Jan. 2021.

[2] X. Chen *et al.*, "Overview of stability research for grid-connected inverters based on impedance analysis method," *Proc. CSEE*, vol. 38, no. 7, pp. 2082–2094, 2018.

[3] L. Xiong, X. Liu, Y. Liu, and F. Zhuo, "Modeling and stability issues of voltage-source converter dominated power systems: A review," *CSEE J. Power Energy Syst.*, pp. 1–18, Nov. 2020, doi: 10.17775/CSEE-JPES.2020.03590.

[4] B. Wen *et al.*, "Analysis of D-Q small-signal impedance of grid-tied inverters," *IEEE Trans. Power Electron.*, vol. 31, no. 1, pp. 675–687, Jan. 2016.

[5] Z. Zou, R. Rosso, and M. Liserre, "Modeling of the phase detector of a synchronous-reference-frame phase-locked loop based on second-order approximation," *IEEE J. Emerg. Sel. Topics Power Electron.*, vol. 8, no. 3, pp. 2534–2545, Sep. 2020.

[6] Z. Zou and M. Liserre, "Study of phase-locked-loop-based synchronization of grid inverter during large phase jump," in *Proc. IEEE Energy Convers. Congr. Expo.*, Portland, OR, USA, 2018, pp. 7128–7134.

[7] Z. Zou and M. Liserre, "Modeling phase-locked loop-based synchronization in grid-interfaced converters," *IEEE Trans. Energy Convers.*, vol. 35, no. 1, pp. 394–404, Mar. 2020.

[8] Z. Zeng *et al.*, "Simplified small-signal modeling method of Grid-connected inverters and its applications," *Proc. CSEE*, vol. 40, no. 21, pp. 7002–7012, Mar. 2020.

[9] X. Wang, L. Harnefors, and F. Blaabjerg, "Unified impedance model of grid-connected voltage-source converters," *IEEE Trans. Power Electron.*, vol. 33, no. 2, pp. 1775–1787, Feb. 2018.

[10] F. Cavazzana, A. Khodamoradi, H. Abedini, and P. Mattavelli, "Analysis of an impedance modeling approach for droop-controlled inverters in system DQ frame," in *Proc. IEEE Energy Convers. Congr. Expo.*, Baltimore, MD, USA, 2019, pp. 5576–5583.

[11] S. Wang, "Terminal-characteristics based small-signal modeling and stability analysis for parallel droop-controlled inverter system," *J. Power Supply*, vol. 18, no. 2, pp. 83–94, Feb. 2020.

[12] Z. Liu, J. Liu, D. Boroyevich, R. Burgos, and T. Liu, "Small-signal terminal-characteristics modeling of three-phase droop-controlled inverters," in *Proc. IEEE Energy Convers. Congr. Expo.*, Milwaukee, WI, USA, 2016, pp. 1–7.

[13] Z. Zou, B. D. Besheli, R. Rosso, M. Liserre, and X. Wang, "Interactions between two phase-locked loop synchronized grid converters," *IEEE Trans. Ind. Appl.*, vol. 57, no. 4, pp. 3935–3947, Jul./Aug. 2021.

[14] R. Rosso, S. Engelken, and M. Liserre, "Robust stability investigation of the interactions among grid-forming and grid-following converters," *IEEE J. Emerg. Sel. Topics Power Electron.*, vol. 8, no. 2, pp. 991–1003, Jun. 2020.

[15] R. Rosso, G. Buticchi, M. Liserre, Z. Zou, and S. Engelken, "Stability analysis of synchronization of parallel power converters," in *Proc. IECON - 43rd Annu. Conf. IEEE Ind. Electron. Soc.*, Beijing, China, 2017, pp. 440–445.

[16] R. Rosso, S. Engelken, and M. Liserre, "Analysis of the parallel operation between synchronverters and PLL-based converters," in *Proc. IEEE Energy Convers. Congr. Expo.*, Baltimore, MD, USA, 2019, pp. 2583–2590.

[17] R. Rosso, M. Andresen, S. Engelken, and M. Liserre, "Analysis of the interaction among power converters through their synchronization mechanism," *IEEE Trans. Power Electron.*, vol. 34, no. 12, pp. 12321–12332, Dec. 2019.

[18] W. Cao *et al.*, "Harmonic stability analysis for multi-parallel inverter-based grid-connected renewable power system using global admittance," *Energies*, vol. 12, no. 14, pp. 3015–3019, Jul. 2019.

[19] H. Tao, H. Hu, X. Wang, F. Blaabjerg, and Z. He, "Impedance-based harmonic instability assessment in a multiple electric trains and traction network interaction system," *IEEE Trans. Ind. Appl.*, vol. 54, no. 5, pp. 5083–5096, Sep./Oct. 2018.

[20] S. Wang, Z. Liu, J. Liu, D. Boroyevich, and R. Burgos, "Small-signal modeling and stability prediction of parallel droop-controlled inverters based on terminal characteristics of individual inverters," *IEEE Trans. Power Electron.*, vol. 35, no. 1, pp. 1045–1063, Jan. 2020.

[21] W. Du *et al.*, "Modeling of grid-forming and grid-following inverters for dynamic simulation of large-scale distribution systems," *IEEE Trans. Power Del.*, vol. 36, no. 4, pp. 2035–2045, Aug. 2021.

[22] D. Pattabiraman, R. H. Lasseter, and T. M. Jahns, "Comparison of grid following and grid forming control for a high inverter penetration power system," in *Proc. IEEE Power Energy Soc. Gen. Meeting*, Portland, OR, USA, 2018, pp. 1–5.

[23] R. Rosso, X. Wang, M. Liserre, X. Lu, and S. Engelken, "Grid-forming converters: Control approaches, grid-synchronization, and future trends—A review," *IEEE Open J. Ind. Appl.*, vol. 2, pp. 93–109, 2021.

[24] Q. Zhong and G. Weiss, "Synchronverters: Inverters that mimic synchronous generators," *IEEE Trans. Ind. Electron.*, vol. 58, no. 4, pp. 1259–1267, Apr. 2011.

[25] P. Rodríguez, C. Citro, J. I. Candela, J. Rocabert, and A. Luna, "Flexible grid connection and islanding of SPC-based PV power converters," *IEEE Trans. Ind. Appl.*, vol. 54, no. 3, pp. 2690–2702, May/Jun. 2018.

[26] S. D'Arco and J. A. Suul, "Equivalence of virtual synchronous machines and frequency-droops for converter-based microgrids," *IEEE Trans. Smart Grid*, vol. 5, no. 1, pp. 394–395, Jan. 2014.

XINGQI LIU (Student Member, IEEE) was born in China, in 1999. She received the B.S. degree in electrical engineering from Shijiazhuang Tiedao University, Shijiazhuang, China, in 2021. She is currently working toward the M.S. degree in electrical engineering with Southeast University, Nanjing, China. Her research interests include smart transformers and the stability of power converters.

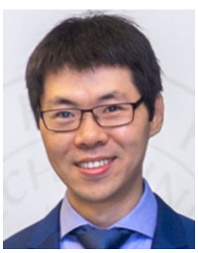

ZHIXIANG ZOU (Senior Member, IEEE) received the B.Eng. and Ph.D. degrees in electrical and engineering from Southeast University, Nanjing, China, in 2007 and 2014, respectively, and the Dr.-Ing. degree (*summa cum laude*) from Kiel University, Kiel, Germany, in 2019. From 2007 to 2009, he was an Engineer with State Grid Electric Power Research Institute, Nanjing, China. From 2014 to 2019, he was a Research Fellow and Lecturer with the Chair of Power Electronics, Kiel University. He is currently an Associate Professor with the School of Electrical Engineering, Southeast University. His research interests include smart transformers, microgrid stability, modeling and control of power converters. Dr. Zou is an Associate Editor for the IEEE OPEN JOURNAL OF POWER ELECTRONICS, an Associate Editor for the IEEE ACCESS, the Editor of the *International Transactions on Electrical Energy Systems*, and the Editor of the *Mathematical Problems in Engineering*, and the Standing Director of the IEEE PES Power System Relaying & Control Satellite Committee.

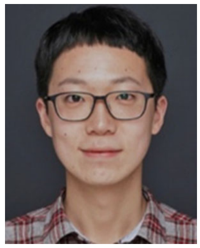

JIAJUN YANG (Student Member, IEEE) received the B.Eng. degree (Hons.) in electrical and electronic engineering in 2017 from the University of Nottingham Ningbo China, Ningbo, China, where he is currently working toward the Ph.D. degree with the Key Laboratory of More Electric Aircraft Technology of Zhejiang Province. From 2017 to 2018, he was a Hardware Engineer with Nottingham Electrification Centre. His current research interests include high power density dc-dc converters and stability analysis of dc microgrids for the more electric aircraft.

JIAN TANG was born in China, in 1999. He received the B.S. degree in electrical engineering in 2021 from Southeast University, Nanjing, China, where he is currently working toward the M.S. degree in electrical engineering. His research interests include the stability of power converters and the application of artificial intelligence on power converters.

ZHIREN LIU received the B.Sc. and M.Sc. degrees from the School of Electrical Engineering, Southeast University, Nanjing, China, in 2007 and 2010, respectively. Since 2010, he has been with Jiangsu Electric Power Company Wuxi Power Supply Company, where he is currently a Senior Engineer. His research interests include power systems, relay protections, and active distribution grids.

GIAMPAOLO BUTICCHI (Senior Member, IEEE) received the master's degree in electronic engineering and the Ph.D. degree in information technologies from the University of Parma, Parma, Italy, in 2009 and 2013, respectively. In 2012, he was a Visiting Researcher with the University of Nottingham, Nottingham, U.K. From 2014 to 2017, he was a Postdoctoral Researcher and a Guest Professor with Kiel University, Kiel, Germany. In 2017, he was appointed as an Associate Professor of electrical engineering with the University of Nottingham Ningbo China, Ningbo, China, and the Head of power electronics of Nottingham Electrification Center. In 2020, he was promoted to a Professor. He is author or coauthor of more than 230 scientific papers. His research interests include power electronics for renewable energy systems, smart transformer fed micro-grids, and dc grids for the more electric aircraft. He is one of the advocates for DC distribution systems and multiport power electronics onboard the future aircraft. Dr. Buticchi is the Chair of the IEEE-IES Technical Committee on Renewable Energy Systems and the IES Energy Cluster Delegate. During his stay in Germany, he was awarded with the Von Humboldt Postdoctoral Fellowship to carry out research related to fault tolerant topologies of smart transformers. He is an Associate Editor for the IEEE TRANSACTIONS ON INDUSTRIAL ELECTRONICS, IEEE TRANSACTIONS ON TRANSPORTATION ELECTRIFICATION, and IEEE Open Journal of the Industrial Electronics Society.

ZHENG WANG (Senior Member, IEEE) received the B.Eng. and M.Eng. degrees from Southeast University, Nanjing, China, in 2000 and 2003, respectively, and the Ph.D. degree from The University of Hong Kong, Hong Kong, in 2008. From 2008 to 2009, he was a Postdoctoral Fellow with Ryerson University, Toronto, ON, Canada. He is currently a Full Professor with the School of Electrical Engineering, Southeast University. He has authored more than 100 internationally refereed papers, one English book by IEEE-Wiley Press, and two English book chapters in his research field, which include electric drives, power electronics, and renewable power generation. Prof. Wang was the recipient of the IEEE PES Chapter Outstanding Engineer Award, Outstanding Young Scholar Award of Jiangsu Natural Science Foundation of China, and several paper awards of journals and conferences. He is an Associate Editor for the IEEE TRANSACTIONS ON INDUSTRIAL ELECTRONICS and *Journal of Power Electronics*.

MING CHENG (Fellow, IEEE) received the B.Sc. and M.Sc. degrees from the Department of Electrical Engineering, Southeast University, Nanjing, China, in 1982 and 1987, respectively, and the Ph.D. degree from the Department of Electrical and Electronic Engineering, University of Hong Kong, Hong Kong, in 2001. Since 1987, he has been with Southeast University, where he is currently a Distinguished Professor with the School of Electrical Engineering and the Director of the Research Center for Wind Power Generation. From January to April 2011, he was a Visiting Professor with the Wisconsin Electric Machine and Power Electronics Consortium, University of Wisconsin, Madison, WI, USA. He has authored or coauthored more than 300 technical papers and four books, and is the holder of 70 patents in his teaching and research field, which include electrical machines, motor drives for EV, and renewable energy generation. Prof. Cheng is a Fellow of the Institution of Engineering and Technology. He was the Chair and an Organizing Committee Member for many international conferences. He is a Distinguished Lecturer of the IEEE Industry Applications Society for 2015/2016.